Check for updates

ADVANCED FUNCTIONAL MATERIALS
www.afm-journal.de

Tuning Rate-Limiting Factors for Graphite Anodes in Fast-Charging Li-Ion Batteries

Yinchao Wang, Yuchen Ji, Zu-Wei Yin, Tian Sheng, Aimin Cao, Wenguang Zhao, Yuxiang Huang, Jun-Tao Li, Feng Pan,* and Luyi Yang**

Localized high-concentration electrolyte (LHCE) is considered to be a promising substitution for the conventional carbonate electrolytes in fast-charging Li-ion batteries. However, the rate-determining steps (RDS) for fast-charging electrodes (i.e., graphite anode) in LHCE remain unclear. Herein, a typical localized high-concentration electrolyte consisting of lithium bis(fluorosulfonyl)imide in dimethoxyethane with 1,1,2,2-tetrafluoroethyl-2,2,3,3-tetrafluoropropyl ether as a diluent is selected to investigate the RDS of lithiation process in graphite anode, including the diffusion of solvated Li^+ in the electrolyte, the desolvation behavior of solvated Li^+, the Li^+ transfer in solid electrolyte interphase (SEI) on the graphite surface, and the Li^+ diffusion in bulk graphite. The results indicated that the rate performance of graphite anode in LHCE lies in the balance between Li^+ desolvation process and Li^+ migration in SEI. Through the regulation of solvated Li^+ structure and SEI component, excellent fast-charging performance can be obtained in the LHCE. The present studies not only offer fresh insights in the mechanistic understanding of fast-charging batteries, but also provide new clues to the performance improvement of graphite anodes.

1. Introduction

The looming depletion of fossil fuels and global climate change urgently require a cleaner energy mix.[1–5] Lithium-ion batteries have been widely used in important fields such as electric vehicles, portable electronic devices, and large-scale energy storage systems.[6–8] Since the advent of lithium-ion batteries in 1991, graphite has firmly maintained its position as the preeminent anode material.[9,10] However, it remains a challenge for lithium-ion batteries using graphite anodes to achieve the fast charging target of 80% in 15 min, which to a certain extent limits the application scenarios of lithium-ion battery applications in real life.[11,12]

In previous studies, the kinetic steps of Li^+ transport in fast-charging lithium-ion batteries can be classified into the following four aspects: 1) solvated Li^+ migration in the electrolyte, 2) desolvation of solvated Li^+ at the electrolyte/SEI interface, 3) Li^+ passing through the solid electrolyte interphase (SEI), and 4) Li^+ diffusion in the graphite bulk.[13–18] In this regard, electrolyte regulation plays a crucial role in the performance of fast-charging lithium batteries, which can affect not only the Li^+ diffusion in bulk electrolyte, but also SEI formation and desolvation energy of solvated Li^+ at SEI/electrolyte interface.

An ideal electrolyte for fast-charging batteries should have: 1) high ionic conductivity, 2) low desolvation energy, and 3) capability to construct high-conductivity SEI to accelerate the Li^+ diffusion from the electrolyte to the graphite particles. These aspects are interrelated and can be tuned through the molecular design of the electrolyte. In recent years, it has been found that graphite electrodes exhibit surprisingly different intercalation behavior in ultra-concentrated organic salt solutions (e.g., salt concentration >3.0 M), forming fewer free solvent molecules in the high-concentration electrolytes (HCEs) compared to conventional electrolytes. Li ions in HCE are forced to share solvent molecules, forming a separate solvation sheath. A large number of anions coordinate with Li ions, which will cause the anions to be preferentially reduced during the formation of SEI on the graphite surface, forming an SEI dominated by inorganic components. The stability and conductivity of inorganic SEI are higher than organic SEI, which makes HCE have excellent fast-charging performance. However, the high viscosity and high cost of HCE are major issues hindering its industrial application.

Inspired by HCEs, localized high-concentration electrolytes (LHCEs) were proposed by diluting the concentrated electrolyte with an inert solvent.[19–21] Consequently, LHCEs can not only regulate the desolvation process of Li^+ and SEI formation, but also lower the viscosity and overall salt concentration. Many studies have proposed LHCEs that can improve the fast-charging performance of graphite anodes, for example, Zhang

Y. Wang, Y. Ji, Z.-W. Yin, A. Cao, W. Zhao, Y. Huang, F. Pan, L. Yang
School of Advanced Materials
Peking University Shenzhen Graduate School
Shenzhen 518055, P. R. China
E-mail: yinzuwei@xmu.edu.cn; panfeng@pkusz.edu.cn; yangly@pkusz.edu.cn
Z.-W. Yin, J.-T. Li
College of Energy
Xiamen University
Xiamen 361005, P. R. China
T. Sheng
College of Chemistry and Materials Science
Anhui Normal University
Wuhu 241000, P. R. China

The ORCID identification number(s) for the author(s) of this article can be found under https://doi.org/10.1002/adfm.202401515

DOI: 10.1002/adfm.202401515

 © 2024 Wiley-VCH GmbH

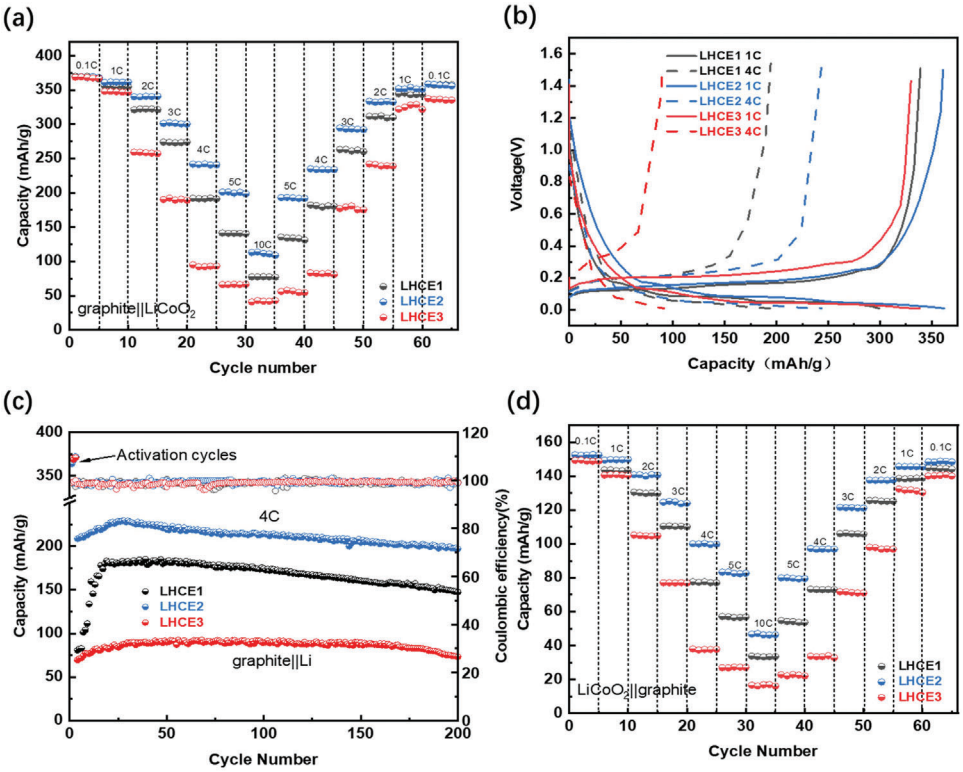

Figure 1. The electrochemical performance using localized high-concentration electrolytes (LHCE1, LHCE2 and LHCE3). a) Rate capability of graphite||Li cells; b) Initial charge-discharge curves at 1 C and 4 C of graphite||Li cells using different electrolytes; c) Cycling performance and Coulombic efficiencies with different electrolytes of graphite||Li cells at 4 C; d) Rate capability of $LiCoO_2$||graphite cells.

et al. proposed a 1.4 M lithium bis(fluorosulfonyl)imide(LiFSI) electrolyte (DMC/EC/TTE, 2:0.2:3 by mol) to achieve fast charging of NCM811||graphite.[22] And Zhang et al. proposed that a localized high-concentration electrolyte consisting of 1.5 M LiFSI in dimethoxyethane with bis(2,2,2-trifluoroethyl) ether as the diluent, enables fast-charging of working batteries.[20] Previous studies have revealed that anions in the solvation structure of LHCE will participate in the coordination of Li^+, thereby forming a uniform and strong SEI on the graphite surface, inhibiting the co-insertion of solvent into graphite, and achieving highly reversible intercalation/deintercalation of Li^+. However, there is a lack of systematic kinetic studies, and the potential mechanism by which LHCE improves the fast-charging performance of graphite remains unclear.

Herein, the charging (lithiating) process of graphite anodes in LHCE was studied from four aspects, including solvated Li^+ migration in the electrolyte, Li^+ desolvation, Li^+ transfer through the SEI, and Li^+ diffusion in the graphite bulk. Combining theoretical calculations with experimental studies, it is revealed that the limiting steps for LHCE to achieve fast-charging graphite rest with the interplay between Li^+ desolvation process on the SEI surface and the process of Li^+ passing through the SEI. Both processes can be optimized by tuning the solvation structure of LHCE. These findings can provide guidance for the future design of fast-charging electrolytes.

2. Result and Disscussion

2.1. Electrochemical Performance of Fast-Charging Graphite Anodes in Localized High-Concentration Electrolytes

The three electrolytes mainly studied in this article are LHCE1 (n_{LiFSI}:n_{DME}:n_{TTE} = 0.4:1:1.4), LHCE2 (n_{LiFSI}:n_{DME}:n_{TTE} = 0.5:1:1.4), LHCE3 (n_{LiFSI}:n_{DME}:n_{TTE} = 0.6:1:1.4), where $c_{LiFSI\text{-}LHCE3}$>$c_{LiFSI\text{-}LHCE2}$>$c_{LiFSI\text{-}LHCE1}$. A low-concentration electrolyte (LCE, component is LiFSI:DME:TTE = 0.1:1:1.4) was selected as a comparison group. In order to evaluate the fast-charging and long-cycle performance of graphite anodes under different electrolytes, galvanostatic discharge/charge tests were carried out on graphite||Li batteries. Figure S1a (Supporting Information) shows the long-cycle performance of the graphite||Li batteries with LCE at 1 C, where a rapid fading of battery capacity using LCE can be seen. The initial capacity of the cell with LCE is only 80 mAh g^{-1}, and the capacity retention rate of 200 cycles is only 38.6%. Figure S1b (Supporting Information) displays the capacity-voltage curves of the graphite||Li battery with LCE, it can be seen that the battery has poor reversibility and low Coulomb efficiency, possibly due to the decomposition and co-intercalation of solvent molecules accompanied by a decrease in potential, resulting in subsequent exfoliation of graphite.[20] which means the electrolyte system is not suitable for graphite anode materials at low concentrations. **Figure 1a** demonstrates the rate performance of three LHCEs. At lower

 © 2024 Wiley-VCH GmbH

16163028, 2024, 29, Downloaded from https://onlinelibrary.wiley.com/doi/10.1002/adfm.202401515 by University Town Of Shenzhen, Wiley Online Library on [28/12/2024]. See the Terms and Conditions (https://onlinelibrary.wiley.com/terms-and-conditions) on Wiley Online Library for rules of use; OA articles are governed by the applicable Creative Commons License

rates, the disparities in capacity among the three electrolytes are relatively inconspicuous. However, with the increase in rate, LHCE2 shows a capacity significantly higher than the other two electrolytes. Battery capacities using LHCE1, LHCE2, and LHCE3 electrolytes were 192, 242, and 95 mAh g^{-1} at 4 C, respectively. From above, the graphite||Li battery using LHCE2 showed a more symmetrical performance curve, indicating that it is more suitable for fast charging of graphite. Figure 1b exhibits capacity-voltage curves of the batteries using LHCE1, LHCE2, and LHCE3 at 1 C and 4 C. Among them, several voltage plateaus appear below ≈0.2 V at 1 C, which is characteristic of the continuous formation of multi-stage structures of LiC_x. Obviously, the reversible capacity obtained with LHCE2 is the highest (364 mAh g^{-1} at 1 C). However, as the rate is increased to 4 C, the voltage plateaus of the cells using LHCE1 and LHCE3 disappeared, while those of the cells using LHCE remained prominent, indicating that the LHCE2 system can adequately supply Li^+ in the rate-determining step of intercalation. The graphite||Li cell with LHCE1, LHCE2, and LHCE3 has good initial capacity and capacity retention rate at 1 C (Figure S2a, Supporting Information). The graphite||Li batteries with LHCE2 also have excellent cycling stability at high rates of 4 C, maintaining a capacity retention rate of 92.1% even after 200 cycles (Figure 1c). It is worth mentioning that compared with a commonly used ester electrolyte, LHCE2 also shows better initial capacity and good cycle stability at 4 C (Figure S3, Supporting Information).

In order to estimate the fast-charging performances of three electrolytes in full cells, galvanostatic discharge/charge tests were carried out on $LiCoO_2$||graphite batteries. As depicted in Figure 1d, the $LiCoO_2$||graphite cells with LHCE2 exhibits good rate capability, especially when they can deliver a high capacity of 104 mAh g^{-1} at 4 C. In comparison, the cells using LHCE1 and LHCE3 possess poor rate performance and only deliver a capacity of 80 and 40 mAh g^{-1}, respectively at 4 C. Figure S2c (Supporting Information) shows the capacity–voltage curves of the batteries with LHCEs, several voltage plateaus appear below ≈3.7 V at 1 C. However, as the rate is increased to 4 C, the voltage plateaus of the cells using LHCE1 and LHCE3 disappeared, while those of the cells using LHCE2 remained prominent, indicating that the LHCE2 system can adequately supply Li^+ in the rate-determining step of intercalation. Figure S2b,d (Supporting Information) demonstrate the cycling performance and Coulombic efficiency of the $LiCoO_2$||graphite batteries with LHCE1, LHCE2, and LHCE3 at 1 C and 4 C respectively. It can be seen that the capacity does not show a significant difference at 1 C and all the cells show good capacity retention rates. Unfortunately, only LHCE2 has a high initial capacity and capacity retention rate at 4 C.

2.2. Diffusion of Li^+ in Electrolytic Liquid and Graphite Bulk

In order to explore the Li^+ diffusion behaviors in different electrolytes, the viscosity and ionic conductivity of various electrolytes were tested. **Figure** 2a provides a depiction of the viscosity profiles across various electrolytes. As the concentration increases, the viscosity of the electrolyte gradually slightly increases. Although LHCE exhibits higher viscosity than LCE, even the highest concentration of LHCE3 has lower viscosity than traditional non-aqueous electrolytes (1 M $LiPF_6$/EC/DMC) due to the presence of diluent.[23] So we believe that the presence of diluent prevents the electrolyte from affecting fast-charging performance due to excessive viscosity. In order to further prove that the LHCE system will not cause big differences in Li^+ diffusion due to viscosity, we conducted contact angle tests on three LHCEs. As depicted in Figure 2b, it can be seen that none of the three LHCEs showed obvious contact angles. It is worth mentioning that during the contact angle test, the electrolyte spread instantly on the electrode surface upon contact and results in low contact angles (Figure 2b), showing that all three electrolytes exhibit good wetting properties on the electrode surface, with no significant differences.

To further study the performance of Li^+ of the three LHCEs during electrolyte liquid phase propagation, the ionic conductivities of the four electrolytes were tested. As displayed in Figure 2c, the ionic conductivities of LCE, LHCE1, LHCE2 and LHCE3 are 13.30, 10.13, 9.82, and 9.64 mS cm^{-1}, respectively. This means that as the lithium salt concentration increases, the ionic conductivity of the electrolyte does not increase monotonically, and the maximum conductivity is the result of a trade-off between the number of carriers and the ionic mobility of these carriers.[24] It can be seen that although the ionic conductivity of the three LHCEs is slightly lower than that of the LCE, the difference in the ionic conductivities of the three LHCEs is negligible, manifesting that the ionic conductivity of electrolyte is not the main reason leading to the different fast-charging performance in LHCEs. In addition to the propagation in the electrolyte liquid phase, the propagation of Li^+ in the graphite bulk phase is also important, so Galvanostatic Intermittent Titration Technique (GITT) tests were conducted on graphite anodes using the three LHCE electrolytes. As demonstrated in previous studies.[17,25] GITT was a typical method to evaluate the Li^+ diffusion rate in bulk electrodes of batteries. Figure 2d exhibits the GITT results for graphite anodes in the three LHCE electrolytes. It can be observed that the GITT results of the three electrolytes do not show distinct differences during the discharge process, indicating that the difference in the diffusion rate of Li^+ in the graphite bulk using the three electrolytes is small.

From above, the Li^+ diffusion processes in the electrolyte liquid and graphite bulk of graphite||Li cells using the three LHCEs are similar, and they are believed to be not associated with the difference of fast-charging performance of graphite anode in LHCEs.

2.3. Ion-Solvent Interaction of Electrolytes

To further explore the interaction between Li-ion and solvent/FSI^- of different electrolytes, Raman spectra of four electrolytes (LCE, LHCE1, LHCE2, and LHCE3) were obtained (**Figure** 3a). Free DME molecules exhibit peaks at 820 and 847 cm^{-1}, corresponding to the CH_2 rocking (ω) and C-O stretching vibrations (ν) of DME, respectively.[26] It is obvious that as the concentration increases, the intensity of the peak corresponding to 847 cm^{-1} gradually decreases, which means that the number of free DME solvent molecules gradually decreases, especially for LHCE3, the peak at 847 cm^{-1} basically disappears

© 2024 Wiley-VCH GmbH

16163028, 2024, 29, Downloaded from https://onlinelibrary.wiley.com/doi/10.1002/adfm.202401515 by University Town Of Shenzhen, Wiley Online Library on [28/12/2024]. See the Terms and Conditions (https://onlinelibrary.wiley.com/terms-and-conditions) on Wiley Online Library for rules of use; OA articles are governed by the applicable Creative Commons License

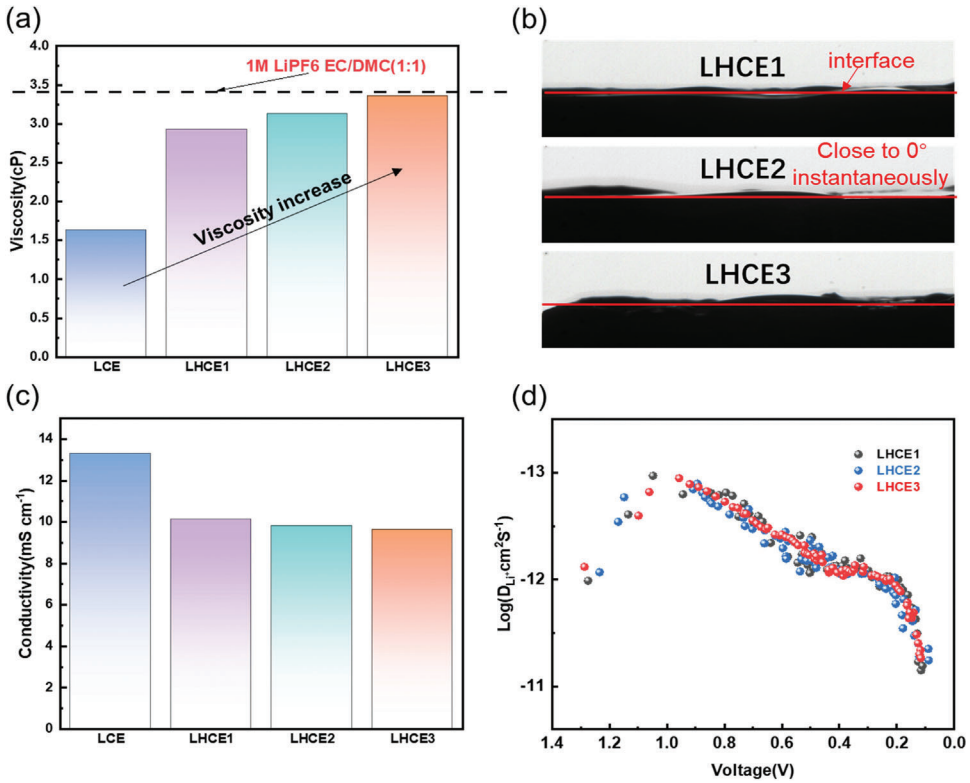

Figure 2. The physicochemical properties of localized high-concentration electrolytes and graphite anode. a) viscosity of the three LHCEs and LCE; b) Contact angles of LHCE1, LHCE2 and LHCE3; c) Li^+ conductivity of the three LHCEs and LCE; d) Li^+ diffusion coefficiencies of graphite anodes at three LHCEs measured by GITT.

in the Raman spectrum of LHCE3. Such results indicate that as the concentration increases, the Li^+ number in the LHCE increases, which leads to the fact that most of the free DME of the solvent will participate in the coordination of Li^+, and part of the FSI^- will also participate in the coordination, enabling the participation of FSI^- in the SEI formation, and favoring the production of a higher proportion of inorganic components. At ≈875 cm^{-1}, a supplementary vibrational peak emerges, which is attributed to the coordination of Li^+ with DME. This peak's intensity exhibits an upward surge in tandem with elevated salt concentration. The similar results can be observed in the infrared spectrum (Figure S4, Supporting Information). Generally, free DME molecules have a peak at 1100 cm^{-1}. As the concentration increases, the intensity of the peak corresponding to 1100 cm^{-1} gradually decreases, which also proves that the number of free DME solvent molecules gradually decreases. Figure 3b shows the ^7Li NMR spectra of the four electrolytes. It clearly indicates that the ^7Li peak of LHCE2 has the most obvious shift, which also means that the Li^+ shielding effect in the LHCE2 electrolyte is the strongest. Because the shielding effect of anions on Li^+ is stronger than that of solvent molecules,[27] it can be concluded that the coordination between Li^+ and FSI^- is in LHCE2 is stronger than LHCE1 due to the increased concertation of anions. Interestingly, shielding effect of LHCE2 is also higher than LHCE3 although the FSI^- in LHCE3 is increased. It is speculated that excessive FSI^- changes the Li^+ coordination structure with DME solvents, which will be verified via simulation in the later part. It should be noted that the most significant ^7Li shift does not necessarily imply the highest desolvation energy. The coordination structures of Li^+ and the desolvation energy in the three electrolytes will be discussed below based on the calculation results.

Next, three-electrode in situ electrochemical impedance spectroscopy (EIS) tests of graphite in LHCEs were conducted to investigate the differences in Li^+ desolvation in different solvation structures. Figure S5 (Supporting Information) shows the impedance spectrum and equivalent fitted circuit of the graphite electrode using LHCE2 at 0.01 V. The in situ impedance test of 1.5–0.01 V was conducted on the graphite electrode using the three-electrode device at 0.1 C and 4 C, repectively. We listed the in situ impedance test results in Tables S1 and **S2** (Supporting Information) based on the circuit model in Figure S5 (Supporting Information). Figure 3c,d demonstrate the charge transfer resistance (R_{ct}) during discharge of graphite anodes in the three electrolytes at 0.1 C for SEI formation and 4 C fast-charing (after 3-cycle activation at 0.1 C as electrochmeical performance test) respectively. It can be seen that whether in the discharge process of 0.1 C or 4 C, the R_{ct} of LHCE3 is always higher than that of LHCE1 or LHCE2, which shows that the Li^+ desolvation of LHCE3 is the most difficult and the Li^+ desolvation might be the RDS in LHCE3. In order to reveal the differences in solvation structures in LHCEs, theoretical calculations were performed on LHCEs. As shown in Figure 3e and Figure S6 (Supporting Information), there are basically no TTE molecules adjacent to

© 2024 Wiley-VCH GmbH

16163028, 2024, 29, Downloaded from https://onlinelibrary.wiley.com/doi/10.1002/adfm.202401515 by University Town Of Shenzhen, Wiley Online Library on [28/12/2024]. See the Terms and Conditions (https://onlinelibrary.wiley.com/terms-and-conditions) on Wiley Online Library for rules of use; OA articles are governed by the applicable Creative Commons License

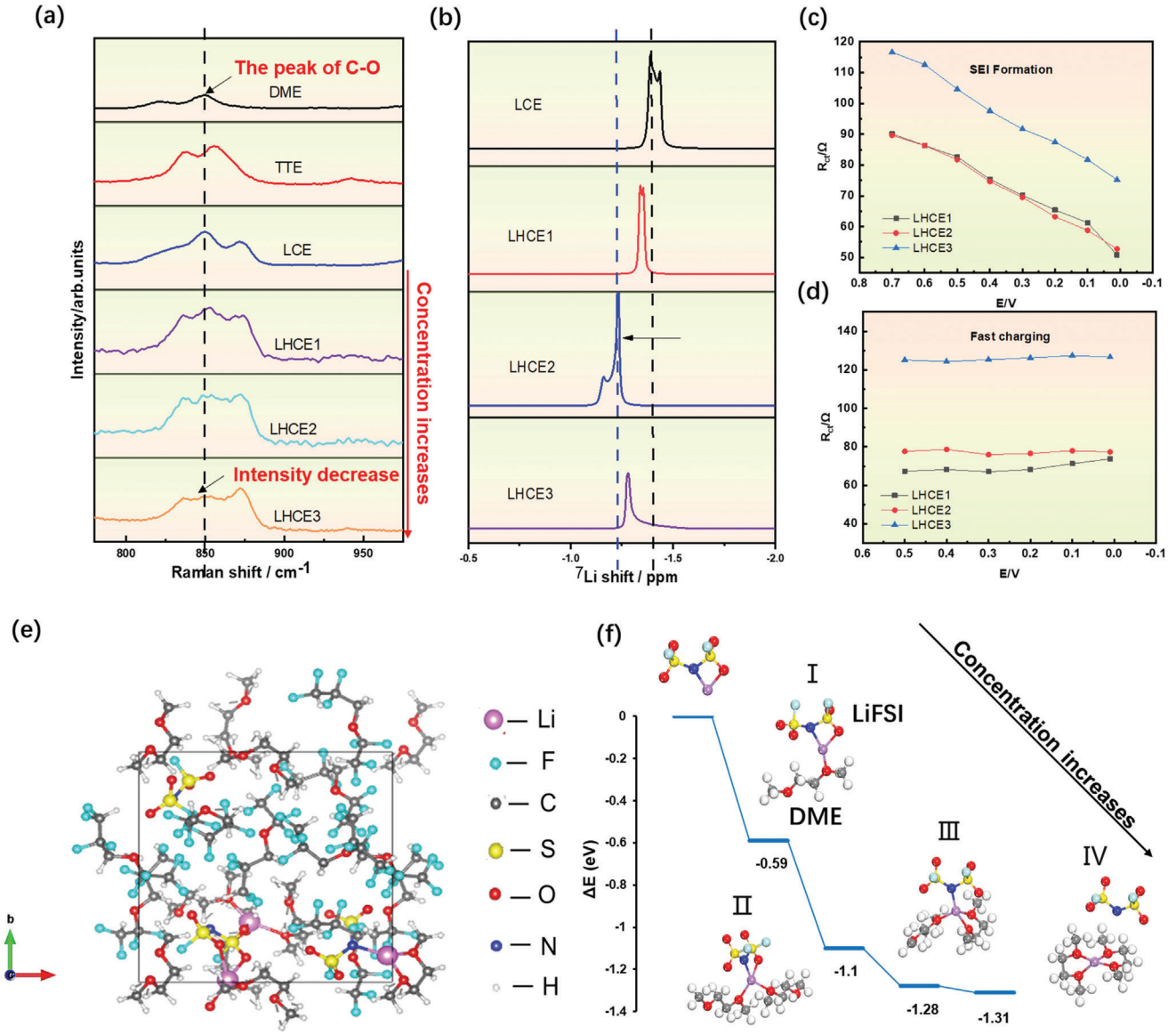

Figure 3. Solvation structure of three localized high-concentration electrolytes and their role in desolvation. a) Raman spectra of LCE, LHCEs, solvent, and diluent; b) ^{7}Li NMR of LCE, LHCE1, LHCE2, LHCE3; The evolution of resistance of charge transfer (R_{ct}) during lithiation of graphite anode at c) 4 C after 3-cycle activation at 0.1 C and d) 0.1 C achieved from three-electrode in situ EIS; e) Solvation structure model of LHCE solution from ab initio molecular dynamics simulations; f) Energy profiles of one FSI^{-} anion substituted by two DME molecules with the optimized structures.

Li^{+}, and Li^{+} is mainly coordianted by FSI^{-} or DME molecules. Figure 3f exhibits the coordination situation in the electrolyte system. In LHCE1, LHCE2, and LHCE3, Li^{+} usually forms a three-coordination or four-coordination structure. The concentration of LHCE1 is higher than that of the traditional electrolyte, and part of the FSI^{-} will participate in Li^{+} coordination, forming a coordination structure in which Li^{+} coordinates with 1 FSI^{-} and 2 DME molecules (II and III). As the concentration increases to LHCE2, more FSI^{-} participates in the coordination of Li^{+}. Due to the strong shielding effect of FSI^{-} on Li^{+}, the most displacement of the ^{7}Li peak in the NMR spectrum occurs in LHCE2. In LHCE3, as the number of Li^{+} continues to increase, there are insufficient free DME molecules in the solvent, and some Li^{+} will combine with the four oxygen atoms in the two DME molecules to form a four-coordination structure (Figure 3f and IV). Due to this coordination, the lack of FSI^{-} with strong shielding ability in the structure leads to a decrease in the overall shielding effect of LHCE3 on Li^{+}. This explains why the ^{7}Li peak shift in the NMR spectrum of LHCE3 is smaller than that of LHCE2 (Figure 3b). It is worth mentioning that the binding energy of the coordination structure (Figure 3f and IV) appearing in LHCE3 is −1.31 eV, which is the highest among all coordination structures. Therefore, LHCE3 shows a higher desolvation energy than LHCE1 and LHCE2.

Overall, combining the experimental results (Raman, IR, NMR, in situ EIS) and theoretical calculation, the Li^{+} of the three

© 2024 Wiley-VCH GmbH

16163028, 2024, 29, Downloaded from https://onlinelibrary.wiley.com/doi/10.1002/adfm.202401515 by University Town Of Shenzhen, Wiley Online Library on [28/12/2024]. See the Terms and Conditions (https://onlinelibrary.wiley.com/terms-and-conditions) on Wiley Online Library for rules of use; OA articles are governed by the applicable Creative Commons License

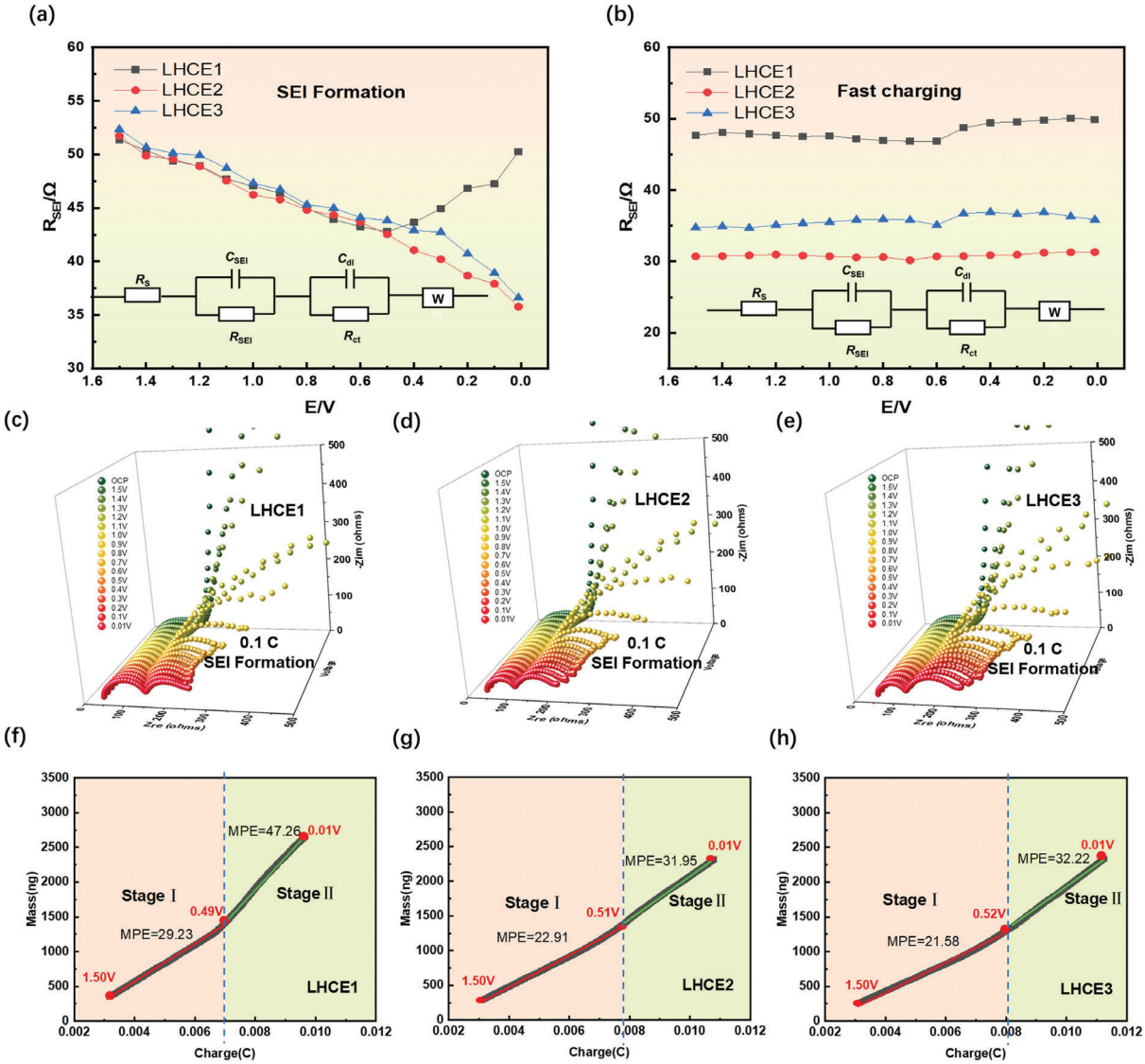

Figure 4. The effect of three localized high-concentration electrolytes on SEI formation. The evolution of resistance of SEI (R_{SEI}) during lithiation of graphite anode at a) 4 C after 3-cycle activation at 0.1 C and b) 0.1 C achieved from three-electrode in situ EIS; in situ EIS plots of graphite in c) LHCE1, d)LHCE2 and e) LHCE3 electrolyte during first discharge at 0.1 C; *MPE* values of first lithiation for graphite in f) LHCE1, g) LHCE2 and h) LHCE3 electrolyte obtained from EQCM measurements, respectively.

LHCEs are mainly coordinated with DME and FSI^-. Among them, most Li^+ in LHCE2 are coordinated with 2 DME and 1 FSI^-. Therefore, FSI^- will decompose preferentially during the generation of SEI on the graphite surface, resulting in a higher proportion of inorganic components in SEI. As Li^+ concentration further increases (LHCE3), a structure in which 1 Li^+ and 2 DME molecules are coordinated will appear, exhibiting a higher binding energy as well as a higher desolvation energy of LHCE3.

2.4. Solid Electrolyte Interphase (SEI) on Fast-Charging Graphite Anode Surface

In order to study the properties of SEI, in situ EIS was conducted. First, three-electrode(graphite/AgCl/Li) in situ EIS testing on the first cycle of the three electrolytes at 0.1 C was performed. **Figure** 4a shows the evolution of resistance of SEI (R_{SEI}) during lithiation of graphite anode at 0.1 C during SEI formation. The corresponding 3D in situ EIS diagrams of LHCE1, LHCE2, and LHCE3 at 0.1 C are depicted in Figure 4c–e, respectively. It can be seen that starting from 0.5 V, the R_{SEI} of LHCE2 and LHCE3 begin to show a downward trend, while the R_{SEI} of LHCE1 displays an upward trend. This indicates that the SEI component generated by LHCE1 after 0.5 V has poor conductivity, which can be ascribed to the organic component generation, LHCE2 and LHCE3 generated better conductive inorganic SEI at this stage. The 3D in situ EIS diagrams of LHCE1, LHCE2, and LHCE3 at 4 C are depicted in Figure S7a–c (Supporting Information). The evolution of resistance of SEI during lithiation of graphite anode at 4 C fast-charing obtained through in situ EIS (Figure 4b) also

 © 2024 Wiley-VCH GmbH

16163028, 2024, 29, Downloaded from https://onlinelibrary.wiley.com/doi/10.1002/adfm.202401515 by University Town Of Shenzhen, Wiley Online Library on [28/12/2024]. See the Terms and Conditions (https://onlinelibrary.wiley.com/terms-and-conditions) on Wiley Online Library for rules of use; OA articles are governed by the applicable Creative Commons License

shows that LHCE2 achieves the smallest R_{SEI}, allowing fast Li^+ transfer across the SEI.

Then, the first-cycle electrochemical quartz crystal microbalance (EQCM) tests on three LHCEs at 0.1 C were conducted to unveil the different SEI formation processes. Figure S8 (Supporting Information) exhibits the mass increase of graphite anodes in the three LHCEs. It is obvious that the mass increase in LHCE1 is the highest, while that of LHCE2 is the least. Figure 4f–h demonstrates the changes in mass accumulated per mole of electron transferred (*MPE*)[28,29] values in the three electrolytes during the EQCM test. It can be seen that the growth process of SEI during the first cycle can be mainly divided into two stages, Stage I (1.5–0.5 V) and Stage II (0.5–0.01 V). At Stage I, the *MPE* value of LHCE2 and LHCE3 is 22.91 and 21.58 g mol^{-1} respectively, which are close to the transfer charge amount of 26 g mol^{-1} for LiF, so we believe that LHCE2 and LHCE3 mainly produce LiF at this stage. By sharp contrast, the *MPE* value of LHCE1 at Stage I is significantly higher than 26 g mol^{-1}. It is possible that at this stage, LHCE1 will also undergo organic reactions in addition to the LiF reaction. At Stage II, LHCE1 also displays a much higher *MPE* value than LHCE2 and LHCE3. We believe that LHCE1 generated a greater proportion of organic SEI during this process, which may be the reason why the R_{SEI} of LHCE1 is significantly higher than that of LHCE2 and LHCE3.

To verify the results revealed by EQCM, X-ray photoelectron spectroscopy (XPS) was used to identify the specific composition of SEI on the graphite anode surface. From the XPS results (**Figure 5a–c**, Figure S9, Supporting Information) of the SEIs derived from LHCE1, LHCE2 and LHCE3, significantly different chemical components can be observed: LHCE2 results in much higher contents of Li_3N and LiF than those of LHCE1 and LHCE3. The same results can also be observed at a different depth (Figure S10, Supporting Information). To further quantitatively analyze the composition of SEI, we performed time-of-flight secondary ion mass spectrometry (TOF-SIMS) analysis on three samples (Figure 5d–g; Figure S11a–d, Supporting Information). It can be seen that among the three LHCEs, LiF and Li_3N are the two main inorganic components in SEI. Specifically, the LiF_2^- intensity of LHCE2 is higher than that of LHCE1 and LHCE3, and the Li_2N^- intensity of LHCE2 and LHCE3 is higher than LHCE1. For the organic CH_2^- component, its intensity in LHCE1 is significantly higher than that of LHCE2 and LHCE3 (Figure 5f).

The energy barrier of Li^+ crossing the SEI process was evaluated by calculating the ion migration energy of the SEI components based on the crystal structures of different SEI components (Figure S12, Supporting Information). Figure 5h shows the migration energies of each component, the calculation results showed that Li_3N has the lowest migration energy. As the highest-proportion lithium salt component in SEI, LiF displays the highest Li^+ migration energy (Figure 5h), but the Li^+ can diffuse through its grain boundaries. The mean square root displacement (MSD) calculations of LiF indicate that the Li^+ diffusion capability increases accompanying the LiF domain size decreases (Figure S13, Supporting Information), manifesting that increase of grain boundaries benefits the Li^+ migraion through LiF. With abundant inorganic species with high Li^+ conductivity (e.g., Li_3N) and species that promote interfacial Li^+ conduction (LiF),[30] the SEI obtained in LHCE2 is favorable for Li^+ migration, which causes the LHCE2 exhibit the lowest R_{SEI}. Figure 5i–k demonstrates the cryo-TEM images of cycled graphite anode in LHCE2 electrolyte. After 3 cycles at 0.1 C, the SEI is uniformly distributed on the graphite surface (Figure S14, Supporting Information), and the thickness of SEI is ≈15 nm (Figure S15a, Supporting Information). The (003) plane of graphite can be clearly observed (Figure S15b, Supporting Information), while the SEI component near the surface are mainly LiF, Li_3N, and amorphous organic species (Figure 5i; Figure S15c,d, Supporting Information), which is consistent with the TOF-SIMS results. Figure 5j,k displays the high-resolution image of region A and B, the corresponding fast Fourier transform (FFT) clearly indicates the formation of crystalline LiF and Li_3N in SEI (Figure 5i).

Overall, due to differences in solvation structures, the three electrolytes differ in the process of forming SEI. Among them, the inorganic components LiF and Li_3N in the SEI components of LHCE2 and LHCE3 are higher than those of LHCE1. The low ion migration energy of Li_3N and the unique crystal structure of LiF in LHCE2 and LHCE3 facilitates fast Li^+ transfer by showing lower R_{SEI} than LHCE1. Hence, the rate-determining step that restricts the fast-charging performance of LHCE1 is the process of Li^+ passing crossing the SEI.

2.5. Rate-Determing Steps of Fast-Charging

Based on the above theoretical and experimental studies, the RDS of graphite fast charging in LHCE is summarized as follows (**Figure 6**). We found that there are two main rate-determining steps associated with LHCEs: 1) desolvation of solvated Li^+ and 2) Li^+ transfer through the SEI. When the concentration is low (LHCE1), the desolvation energy barrier of Li^+ is low, while the resistance of the SEI formed on the graphite surface is large due to the organic-rich SEI. As a result, the process of Li^+ passing through the SEI becomes the RDS. As the concentration increases (LHCE2), an inorganic-rich SEI with low resistance is formed on the graphite surface, while the desolvation energy of Li only increases slightly. In this case, both steps are kinetically matched for fast-charging, so LHCE2 has the best fast-charging performance. As the concentration continues to increase (LHCE3), the resistance of the SEI formed on the graphite surface remains small, but the desolvation energy of Li^+ increases significantly. Hence, the desolvation process of solvated Li^+ becomes the RDS. Since the RDS for fast charging depends on the concentration, the bottlenecking effect can be circumvented by selecting a moderate concentration.

3. Conclusion

In summary, the kinetic processes of graphite anode in localized high-concentration electrolytes were systematically studied combined with theoretical calculations and experimental methods. The research results manifest that in our selected LHCE system, there is little difference in the rate of Li^+ migration in the electrolyte liquid and the diffusion of the graphite bulk phase. In comparison, both the desolvation energy of Li^+ and Li^+ transfer through the SEI processes could be the RDS for fast charging, depending on the concentration. At low concentrations (e.g.,

© 2024 Wiley-VCH GmbH

16163028, 2024, 29, Downloaded from https://onlinelibrary.wiley.com/doi/10.1002/adfm.202401515 by University Town Of Shenzhen, Wiley Online Library on [28/12/2024]. See the Terms and Conditions (https://onlinelibrary.wiley.com/terms-and-conditions) on Wiley Online Library for rules of use; OA articles are governed by the applicable Creative Commons License

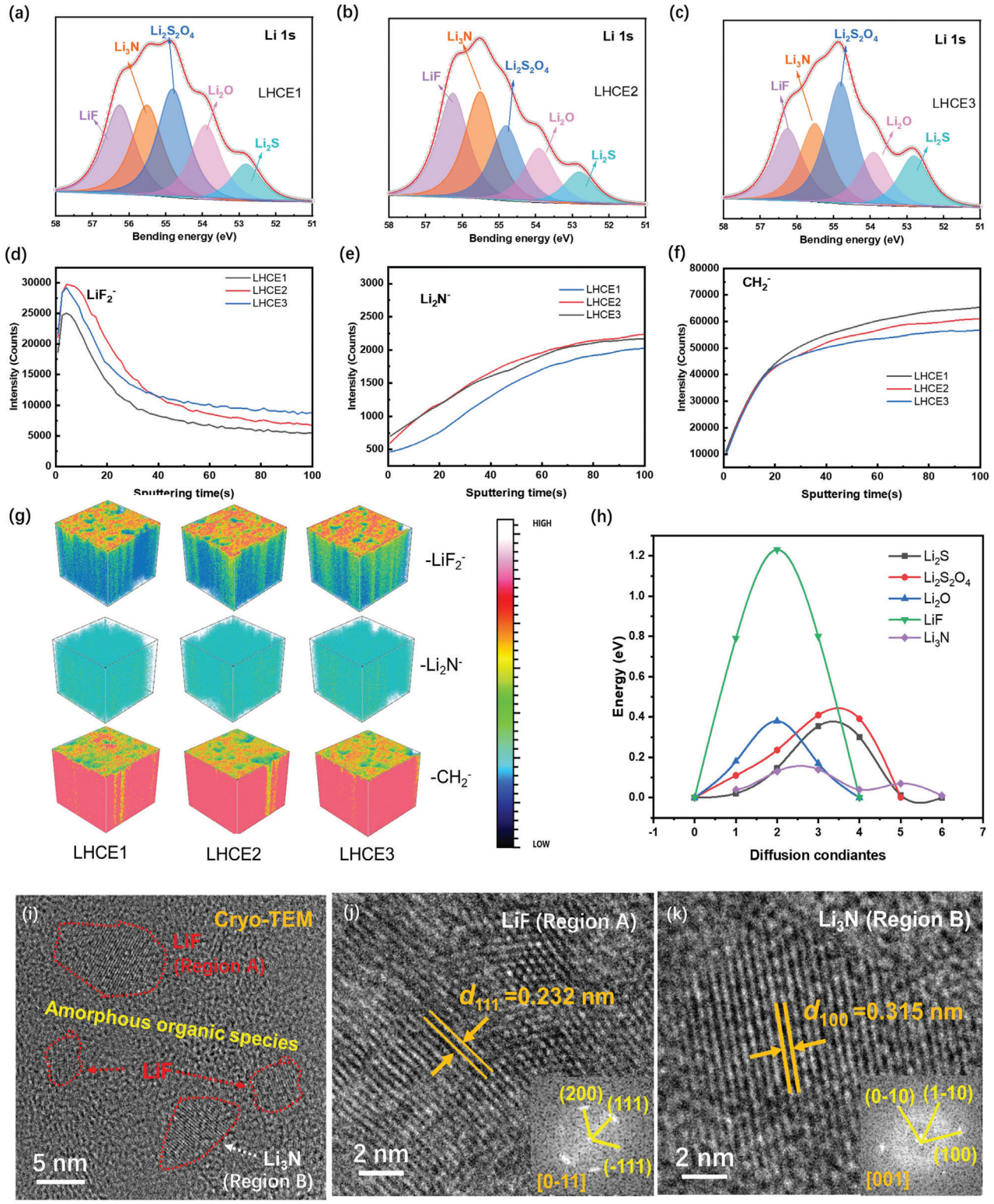

Figure 5. SEI component and properties defination on graphite anode. Li 1s spectra of lithiated graphite surface of a) LHCE1, b) LHCE2, and c) LHCE3; The normalized TOF-SIMS signal intensities of d) LiF^-, e) Li_2N^-, and f) CH_2^- of the SEI formed in LHCE1, LHCE2 and LHCE3. g) 3D distribution of various components of the inner SEI measured via TOF-SIMS in LHCE1, LHCE2, LHCE3; h) Calculated Li^+ migration energy of different SEI componets (Li_2S, Li_2O, LiF, Li_3N and $Li_2S_2O_4$); Cryo-TEM images of SEI on graphite: i) high-resoluton Cryo-TEM image indicated the LiF, Li_3N and amorpphous organic speciescomponents of SEI, j) Enarge image of region A in (i) indicated the LiF crystal structure, k) Enarge image of region B in (i) indicated the LiF crystal structure.

 © 2024 Wiley-VCH GmbH

16163028, 2024, 29, Downloaded from https://onlinelibrary.wiley.com/doi/10.1002/adfm.202401515 by University Town Of Shenzhen, Wiley Online Library on [28/12/2024]. See the Terms and Conditions (https://onlinelibrary.wiley.com/terms-and-conditions) on Wiley Online Library for rules of use; OA articles are governed by the applicable Creative Commons License

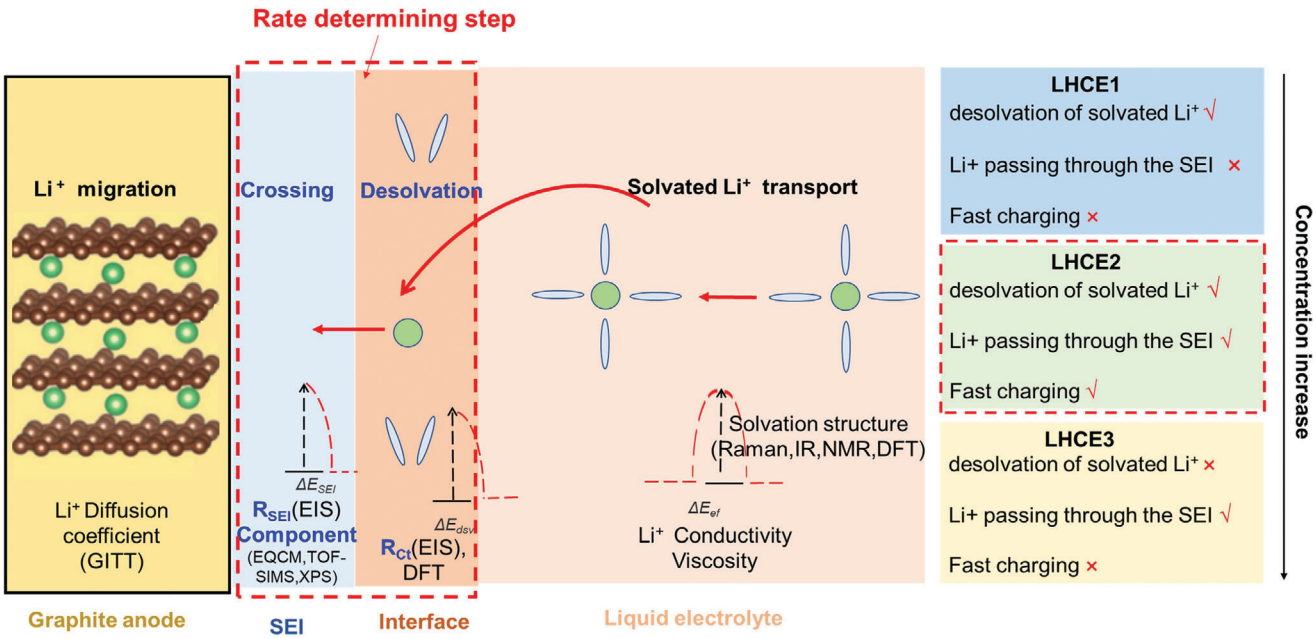

Figure 6. Scheme illustrated the rate-determing steps of graphite anode in localized high-concentration electrolyte, indicating the desolvation and Li^+ diffusion in SEI is kenetic limited steps.

LHCE1), the sluggish Li^+ transfer through SEI is determined to be the RDS. Whereas at excessively high concentrations (e.g., LHCE3), the change in the solvation structure will lead to an increase in the desolvation energy of Li^+, and the RDS of fast charging gradually changes from Li^+ passing through SEI to desolvation of solvated Li^+. Therefore, only by reaching an optimized concentration (e.g., LHCE2), can we achieve the balance of solvated Li^+ desolvation and Li^+ migration in the SEI. Apart from tuning the solvation structure, introducing additives are equally effective in constructing desirable SEI. The Li^+ transport behavior studied in this article is not only applicable to localized high-concentration electrolytes, but also to other electrolyte systems.

Supporting Information

Supporting Information is available from the Wiley Online Library or from the author.

Acknowledgements

Y.W. and Y.J. contributed equally to this work. This work was supported by the National Key Research and Development Program of China (2022YFB2502103), Shenzhen Science and Technology Research Grant (No. ZDSYS201707281026184, JSGG20220831095604008) and Soft Science Research Project of Guangdong Province (2017B030301013), National Natural Science Foundation of China (No. 22309153, No.22288102), Fundamental Research Funds for the Central Universities (No. 20720230039).

Conflict of Interest

The authors declare no conflicts of interest.

Data Availability Statement

Research data are not shared.

Keywords

fast-charging batteries, graphite anode, localized high-concentration electrolyte, rate-determining steps

Received: January 25, 2024
Revised: March 17, 2024
Published online: April 3, 2024

[1] L. A.-W. Ellingsen, C. R. Hung, G. Majeau-Bettez, B. Singh, Z. Chen, M. S. Whittingham, A. H. Strømman, *Nat. Nanotechnol.* **2016**, *11*, 1039.
[2] Y. Song, W. Cai, L. Kong, J. Cai, Q. Zhang, J. Sun, *Adv. Energy Mater.* **2019**, *10*, 1901075.
[3] V. R. Stamenkovic, D. Strmcnik, P. P. Lopes, N. M. Markovic, *Nat. Mater.* **2016**, *16*, 57.
[4] Y. K. Liu, C. Z. Zhao, J. Du, X. Q. Zhang, A. B. Chen, Q. Zhang, *Small* **2022**, *19*, 2205315.
[5] S. Mahmud, M. Rahman, M. Kamruzzaman, M. O. Ali, M. S. A. Emon, H. Khatun, M. R. Ali, *Results Eng.* **2022**, *15*, 100472.
[6] Y. Wang, B. Liu, Q. Li, S. Cartmell, S. Ferrara, Z. D. Deng, J. Xiao, *J. Power Sources* **2015**, *286*, 330.
[7] J. O. B. Gerhard, H. Wrodnigg, M. Winter, *Engineering* **2018**, *4*, 831.
[8] Y. Luo, X. Gao, M. Dong, T. Zeng, Z. Chen, M. Yang, Z. Huang, R. Wang, F. Pan, Y. Xiao, *Chin. J. Struct. Chem.* **2023**, *42*, 100032.
[9] S. Li, K. Wang, G. Zhang, S. Li, Y. Xu, X. Zhang, X. Zhang, S. Zheng, X. Sun, Y. Ma, *Adv. Funct. Mater.* **2022**, *32*, 2200796.
[10] Y. Liang, C. Z. Zhao, H. Yuan, Y. Chen, W. Zhang, J. Q. Huang, D. Yu, Y. Liu, M. M. Titirici, Y. L. Chueh, H. Yu, Q. Zhang, *InfoMat* **2019**, *1*, 6.

© 2024 Wiley-VCH GmbH

16163028, 2024, 29, Downloaded from https://onlinelibrary.wiley.com/doi/10.1002/adfm.202401515 by University Town Of Shenzhen, Wiley Online Library on [28/12/2024]. See the Terms and Conditions (https://onlinelibrary.wiley.com/terms-and-conditions) on Wiley Online Library for rules of use; OA articles are governed by the applicable Creative Commons License

[11] H. Adenusi, G. A. Chass, S. Passerini, K. V. Tian, G. Chen, *Adv. Energy Mater.* **2023**, *13*, 2203307.
[12] S. J. An, J. Li, C. Daniel, D. Mohanty, S. Nagpure, D. L. Wood, *Carbon* **2016**, *105*, 52.
[13] W. Cai, Y.-X. Yao, G.-L. Zhu, C. Yan, L.-L. Jiang, C. He, J.-Q. Huang, Q. Zhang, *Chem. Soc. Rev.* **2020**, *49*, 3806.
[14] M. Weiss, R. Ruess, J. Kasnatscheew, Y. Levartovsky, N. R. Levy, P. Minnmann, L. Stolz, T. Waldmann, M. Wohlfahrt-Mehrens, D. Aurbach, M. Winter, Y. Ein-Eli, J. Janek, *Adv. Energy Mater.* **2021**, *11*, 2101126.
[15] W. Xu, C. Welty, M. R. Peterson, J. A. Read, N. P. Stadie, *J. Electrochem. Soc.* **2022**, *169*, 010531.
[16] H. Zhang, Z. Song, J. Fang, K. Li, M. Zhang, Z. Li, L. Yang, F. Pan, *J. Phys. Chem. C* **2023**, *127*, 2755.
[17] W. Cai, C. Yan, Y.-X. Yao, L. Xu, R. Xu, L.-L. Jiang, J.-Q. Huang, Q. Zhang, *Small Struct.* **2020**, *1*, 2000010.
[18] M. Wang, Q. Sun, Y. Liu, Z. Yan, Q. Xu, Y. Wu, T. Cheng, *Chin. J. Struct. Chem.* **2024**, *42*, 43.
[19] X. Cao, H. Jia, W. Xu, J.-G. Zhang, *J. Electrochem. Soc.* **2021**, *168*, 010522.
[20] L. L. Jiang, C. Yan, Y. X. Yao, W. Cai, J. Q. Huang, Q. Zhang, *Angew. Chem., Int. Ed.* **2020**, *60*, 3402.
[21] J. Hu, Y. Ji, G. Zheng, W. Huang, Y. Lin, L. Yang, F. Pan, *Aggregate* **2022**, *3*, e153.
[22] X. Zhang, L. Zou, Y. Xu, X. Cao, M. H. Engelhard, B. E. Matthews, L. Zhong, H. Wu, H. Jia, X. Ren, P. Gao, Z. Chen, Y. Qin, C. Kompella, B. W. Arey, J. Li, D. Wang, C. Wang, J. G. Zhang, W. Xu, *Adv. Energy Mater.* **2020**, *10*, 2000368.
[23] J. Holoubek, K. Kim, Y. Yin, Z. Wu, H. Liu, M. Li, A. Chen, H. Gao, G. Cai, T. A. Pascal, P. Liu, Z. Chen, *Energy Environ. Sci.* **2022**, *15*, 1647.
[24] G. A. Giffin, *Nat. Commun.* **2022**, *13*, 5250.
[25] J. H. Park, H. Yoon, Y. Cho, C.-Y. Yoo, *Materials* **2021**, *14*, 4683.
[26] L. Qin, N. Xiao, J. Zheng, Y. Lei, D. Zhai, Y. Wu, *Adv. Energy Mater.* **2019**, *9*, 1902618.
[27] Y. Zhao, T. Zhou, T. Ashirov, M. E. Kazzi, C. Cancellieri, L. P. H. Jeurgens, J. W. Choi, A. Coskun, *Nat. Commun.* **2022**, *13*, 2575.
[28] Y. Ji, Z.-W. Yin, Z. Yang, Y.-P. Deng, H. Chen, C. Lin, L. Yang, K. Yang, M. Zhang, Q. Xiao, J.-T. Li, Z. Chen, S.-G. Sun, F. Pan, *Chem. Soc. Rev.* **2021**, *50*, 10743.
[29] Z.-W. Yin, X.-X. Peng, J.-T. Li, C.-H. Shen, Y.-P. Deng, Z.-G. Wu, T. Zhang, Q.-B. Zhang, Y.-X. Mo, K. Wang, L. Huang, H. Zheng, S.-G. Sun, *ACS Appl. Mater. Interfaces* **2019**, *11*, 16214.
[30] S. Tu, B. Zhang, Y. Zhang, Z. Chen, X. Wang, R. Zhan, Y. Ou, W. Wang, X. Liu, X. Duan, L. Wang, Y. Sun, *Nat. Energy* **2023**, *8*, 1365.

© 2024 Wiley-VCH GmbH

16163028, 2024, 29, Downloaded from https://onlinelibrary.wiley.com/doi/10.1002/adfm.202401515 by University Town Of Shenzhen, Wiley Online Library on [28/12/2024]. See the Terms and Conditions (https://onlinelibrary.wiley.com/terms-and-conditions) on Wiley Online Library for rules of use; OA articles are governed by the applicable Creative Commons License